Journal of Volcanology and Geothermal Research 451 (2024) 108113

Contents lists available at ScienceDirect

Journal of Volcanology and Geothermal Research

journal homepage: www.journals.elsevier.com/journal-of-volcanology-and-geothermal-research

How an embryonic magma feeding system evolves: Insights from the primordial pulses of Mt. Etna volcano

Marisa Giuffrida [a], Eugenio Nicotra [b], Marco Viccaro [a,c,*]

[a] Università degli Studi di Catania, Dipartimento di Scienze Biologiche, Geologiche e Ambientali, Corso Italia 57, Catania, Italy
[b] Università della Calabria, Dipartimento di Biologia Ecologia e Scienze della Terra, Via P. Bucci 15/B, Rende, CS, Italy
[c] Istituto Nazionale di Geofisica e Vulcanologia – Sezione di Catania, Osservatorio Etneo, Piazza Roma 2, Catania, Italy

ARTICLE INFO

Keywords:
Etna
Tholeiite
Olivine
Diffusion modeling
Regional tectonics

ABSTRACT

Volcanism at Mt. Etna (Italy) started with an early tholeiitic stage dating back to 542 ka during which subaqueous to subaerial magmas were emitted chiefly through fissure-type eruptions on widespread areas located on the southern flank of the modern volcano edifice. Volcanic products belonging to the earlier Aci Trezza Synthem (542–496 ka) and those of the later Adrano Synthem (332–320 ka) are basalts within a narrow range of variation. Despite the rather homogeneous geochemical characteristics, zoning patterns and Fe—Mg diffusion chronometry on olivine crystals from lavas of both the Synthemic Units have evidenced different dynamics and kinetics of storage and transfer before eruptions. Specifically, one dominant, normally-zoned, $Fo_{83–86}$ olivine population makes peculiar lavas of the Aci Trezza Synthem, whose patterns can be interpreted as due to simple upward migration from deep storage reservoirs directly to the surface with timescales of 109–200 days. Volcanic rocks of the Adrano Synthem have at least three additional olivine populations (i.e., Fo_{78-81}, Fo_{73-74}, Fo_{64-70}) bearing more complex normal and reverse zoning patterns, features revealing that magmas ascended from the deeper storage zones and then intruded and stalled in shallower reservoirs before being erupted. Transfers throughout these magma reservoirs record both short (<46 days) and long timescales (>106 days), suggesting that tectonics could have accelerated or inhibited magma supply during this later stage of volcanic activity. This new dataset points out that the embryonic plumbing system of Mt. Etna developed a more complex architecture throughout the first ~200 ka of volcanism as a consequence of a declining effect of transtensional tectonics over time.

1. Introduction

The onset of Pleistocene volcanism at Mt. Etna, Italy, involved the eruption of tholeiitic to transitional basalts via a system of fractures and faults cutting the eastern Sicily. Subcrustal transtensional faulting and associated fracturing facilitated magma ascent through the lithosphere, as well as the intrusion of subvolcanic bodies at shallow depth, feeding both effusive and explosive fissure eruptions between 542 and 320 ka (Gillot et al., 1994; Hirn et al., 1997; Monaco et al., 1997; Catalano et al., 2004; De Beni et al., 2011). The eruptions of this period are generally referred to a "pre-Etnean volcanism" phase (Rittmann, 1973; Tanguy, 1978), as the volcanic activity occurred before the building of the Mt. Etna central edifice (Tanguy et al., 1997; Branca et al., 2011a, 2011b; De Beni et al., 2011). Early volcanic rocks retain the record of the first evolutionary processes of Etnean magmas and characteristics of the primitive feeding system that evolved into a central-conduit system, while experiencing significant changes towards alkaline magmatic compositions (ca. 130 ka; Ferlito and Nicotra, 2010). At present, these old products crop out discontinuously close to the southern edge of the volcanic edifice. The oldest outcrops date back to 542 ± 85.8 ka (De Beni et al., 2011) and can be observed along the Ionian coast north of Catania, where submarine fissure eruptions of basaltic magmas emplaced mostly pillow lavas, volcanoclastic breccias and hyaloclastites. These products are currently well exposed in the town of Acicastello and Aci Trezza (Figs. 1–2). The youngest outcrops date back to 320.0 ± 48.4 (De Beni et al., 2011) and are distributed on the SW volcano flank in the Adrano-Paternò area, where the fissure activity was essentially subaerial (Figs. 1–2). Here, a subaerial depositional environment developed as a consequence of the tectonic uplift of eastern Sicily that caused the emerging of the Neogene-Quaternary sedimentary basement and the following formation of alluvial terraces and the Simeto river paleo-valley (Monaco et al., 1997; Di Stefano and Branca,

* Corresponding author at: Università degli Studi di Catania, Dipartimento di Scienze Biologiche, Geologiche e Ambientali, Corso Italia 57, Catania, Italy.
E-mail address: marco.viccaro@unict.it (M. Viccaro).

https://doi.org/10.1016/j.jvolgeores.2024.108113
Received 13 February 2024; Received in revised form 30 April 2024; Accepted 24 May 2024
Available online 26 May 2024
0377-0273/© 2024 The Author(s). Published by Elsevier B.V. This is an open access article under the CC BY-NC-ND license (http://creativecommons.org/licenses/by-nc-nd/4.0/).

2002).

Past geochemical studies of both submarine and subaerial rocks combined with field investigations have produced models of magma generation and evolution under variable conditions, highlighting complex eruptive dynamics that have been partially associated with variations of the magma ascent velocity and effects of regional tectonics during these first stages of volcanism (e.g., Cristofolini, 1971, 1972, 1973, 1974; Tanguy, 1978; Cristofolini et al., 1981; Kamenetsky and Clocchiatti, 1996; Corsaro and Cristofolini, 1997, 2000; Clocchiatti et al., 1998). However, despite the past efforts, our knowledge of the early Etnean activity has remained restricted to the origin and emplacement of volcanic rocks, without considering the evolution of magma storage and transfer dynamics over time. Such processes are strictly connected with the architecture of the magma plumbing system, which at Mt. Etna has been a topic largely addressed in the last decades, mostly because of the sudden and continuous changes in the eruptive styles experienced by the volcano in historic and recent times (Branca and Del Carlo, 2005; Corsaro et al., 2009; Di Renzo et al., 2019; Kahl et al., 2013, 2015, 2017; Nicotra and Viccaro, 2012; Viccaro et al., 2016; Giuffrida and Viccaro, 2017; Giuffrida et al., 2021, 2023). The complexity of Mt. Etna eruptive behavior has, however, drove the volcanological attention on factors and processes controlling the most recent magma dynamics, while the interest in the early volcanic manifestations has dropped significantly.

Rocks analyzed in this study belong to the Basal Tholeiitic Supersynthem, according to the modern volcanic stratigraphy proposed by Branca et al. (2004, 2011a, 2011b). The Basal Tholeiitic Supersynthem includes two Synthemic Units, the Aci Trezza Synthem (542 ± 85.8–496.1 ± 86.8 ka; De Beni et al., 2011) and the later Adrano Synthem (332.4 ± 43.4–320.0 ± 48.4 ka; De Beni et al., 2011). The study of the Basal Tholeiitic Supersynthem is mostly based on the analysis and comparison of the whole-rock and mineral chemistry of volcanic products from different eruptions related to both Synthemic Units. The Aci Trezza Synthem is made up by submarine deposits (pillows, columnar lavas, and hydroclastic breccias) emitted by effusive fissure eruptions and hydromagmatic activity on the seafloor of the Gela-Catania foredeep basin during lower-middle Pleistocene (Corsaro and Cristofolini, 2000). The Adrano Synthem includes the subaerial lava flow units and subvolcanic bodies disseminated on the lower southwestern flank of the Etnean edifice (Fig. 1). At present, the occurrence of volcanic manifestations between the two Synthemic Units are uncertain, a feature that has led some authors to suggest a temporal hiatus of ~200 ka during this early stage (Branca et al., 2011a, 2011b).

This study aims at providing new data to explain the distinct

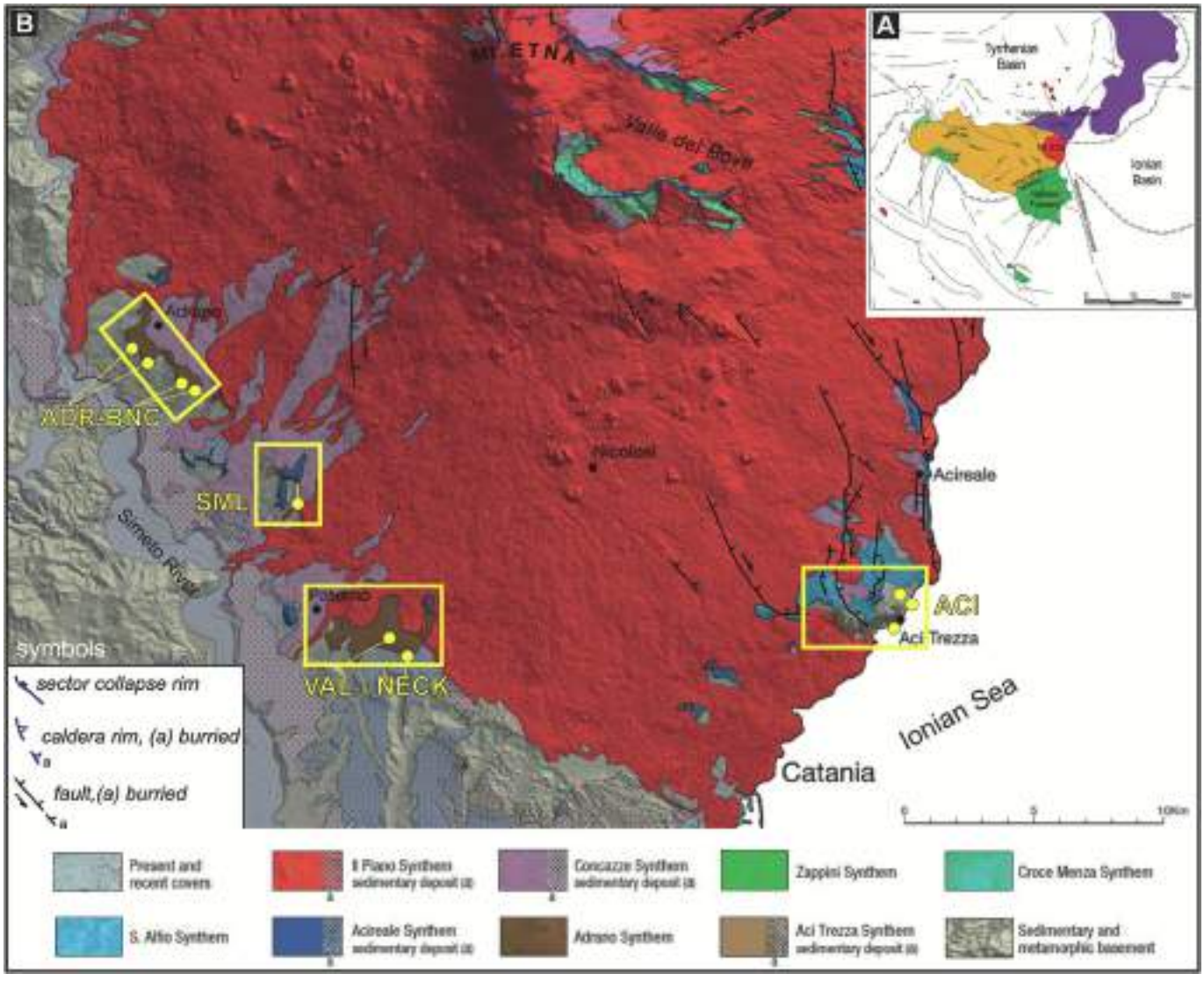

Fig. 1. Map of Mt. Etna volcano (modified after Branca et al., 2011a) showing the location of the sampling points and the distribution of the Etnean tholeiitic units of the Aci Trezza (ACI) and the Adrano (ADR, SML, VAL, BNC, NECK) Synthems.

petrographic characteristics and chemistry of the products related to the early subalkaline magmatism of Mt. Etna, and shed lights on the dynamics of magma supply at that time. With this regard, we use a modern approach based on the combination of thermodynamic modeling on whole-rock and micro-analytical data on volcanic crystals with the aim of gathering clues on the architecture of the ancient plumbing system and put into evidence potential changes in modes and kinetics of magma transport in a period of major geological changes driven by tensional episodes and regional uplift. Because of the ubiquitous presence of olivine in the Basal Tholeiitic Supersynthem lava rocks, the reconstruction of the storage and transport histories of magmas follows the analysis of olivine chemical zoning, whose compositional and temporal record enables to clarify the dynamics that magmas experienced before eruption.

2. Sample description and analytical procedures

Various outcrops related to the Aci Trezza and Adrano Synthems have been investigated in order to find the most suitable locations for rock sampling. The new volcanological survey has led to the collection of eighteen samples of lavas from various locations on the south-eastern and south-western lower flanks of Mt. Etna. The ACI sample dataset is made up by submarine pillow lavas belonging to the oldest eruptive units of the Aci Trezza Synthem (Table 1). These samples were collected in the area between the towns of Acicastello and Aci Trezza (Figs. 1–2), where the submarine lavas are well exposed along the coast. The ancient age of activity, joined to the subaqueous emplacement for volcanic rocks of the Aci Trezza Synthem, results in a certain degree of alteration, being most of the cliffs and outcrops deeply fractured and showing weathering typical of basalts. According to their stratigraphic position, the outcrops can be referred to various cycles of fissure activity within the Aci Trezza Synthem evolution (Corsaro and Cristofolini, 2000; Branca et al., 2008, 2011a, 2011b). For the Adrano Synthem, rock samples were collected at different sites in the municipalities of Adrano (ADR1; ADR2 and ADR3), Biancavilla (BNC1; BNC2 and BNC3), S. Maria di Licodia (SML1a; SML1b and SML2), Valcorrente (VAL3) and Motta Sant'Anastasia (NECK1 to NECK6; Figs. 1–2). ADR, BNC, SML and VAL rocks are referred to a succession of lava flows that filled the Simeto paleo-valley 330–320 ka ago (Branca et al., 2004; De Beni et al., 2011) forming a composite lava flow field that extended for >25 km into the paleovalley and reached the sea in the Valcorrente area (Branca et al., 2008, 2011a, 2011b; Fig. 1). The NECK samples are part of the Motta Sant'Anastasia basaltic neck, today outcropping in the old part of the homonymous town (Figs. 1–2).

All volcanic samples examined in this work were analyzed for whole-rock major elements (Table 1) at the Dipartimento di Scienze della Terra of the University of Calabria (Cosenza, Italy) by means of a Philips PW2404 WD-XRF on powder pellets correcting the matrix effects according to Franzini et al. (1972). Loss on ignition (L.O.I.) was determined by gravimetric methods. On submarine rocks of the Aci Trezza Synthem L.O.I. is >5 wt%, suggesting a certain degree of weathering. The analytical precision and the accuracy of major element concentrations is 2–3%. From the set of eighteen samples, we selected eleven samples on which micro-analytical data on all the mineral phases have been also collected. These samples were inspected on polished thin sections using optical and electron microscopy at the Dipartimento di Scienze Biologiche, Geologiche e Ambientali of the University of Catania. A TESCAN Vega-LMU scanning electron microscope (SEM) equipped with an EDAX Neptune XM4–60 micro-analyzer operating by energy dispersive system (EDS) was used for the microanalysis of minerals. The microscope is equipped with an ultra-thin Be window, and it is coupled with an EDAX WDS LEXS (wavelength dispersive low energy X-ray spectrometer) calibrated for light elements. Operating conditions were set at 20 kV accelerating voltage and 8 nA beam current to acquire high-contrast back-scattered electron images (BSE; 1024 × 864 pixels) and at 20 kV accelerating voltage and 2 nA beam current to obtain major element concentrations of crystals. Repeated analyses on SPI 02753-AB Serial KF certified standard glass during the analytical runs provided precision for all measured elements of around 3%. Accuracy is of the same order of magnitude as precision. Furthermore, major element abundances in olivine crystals were measured along core-to-rim transects on a selection of 61 crystals. Analytical traverses were done

Fig. 2. Sampling sites of the volcanic rocks of the Aci Trezza and Adrano Synthems. A) The Aci Castello rock, a rampart of pillow lavas, pillow breccias and hyaloclastites, belonging to the Aci Trezza Synthem; B) Perpendicular section of two pillow lavas at the base of the Aci Castello rock; C) Panorama of the Aci Trezza area: on the right the Aci Trezza "Faraglioni", two rocks remains of the seawater erosion of the tholeiitic platform of Aci Trezza; D) South-eastern flank of the Motta Sant'Anastasia neck (NECK dataset); E) Columnar joints in the south-western flank of the Motta Sant'Anastasia neck.

Table 1
Major oxide concentrations (wt%) of the Etnean tholeiites belonging to the Aci Trezza and the Adrano Synthems.

	Aci Trezza Synthem		Adrano Synthem														
Sample	ACI1A	ACI1B	ADR1	ADR2	ADR3	BNC1	BNC2	BNC3	SML1A	SML1B	SML2	VAL3	NECK1	NECK2	NECK3	NECK4	NECK5	NECK6
	512,472.9E	512,721.1E	485,400.2E	485301E	485,400.2E	487927E	487725E	487999E	490,265.5E	490270E	490275E	494,312.8E	497036E	497036E	497036E	497036E	497036E	497036E
UTM	4,156,679	4,156,613	4,167,383	4,167,450	4,167,488	4,166,033	4,166,490	4,166,120	4,162,828	416,285	4,162,966	4,156,343	4,151,007	4,151,007	4,151,007	4,151,007	4,151,007	4,151,007
	N	N	N	N	N	N	N	N	N	N	N	N	N	N	N	N	N	N
Location	Acicastello	Acicastello	Adrano	Adrano	Adrano	Biancavilla	Biancavilla	Biancavilla	S.M. di Licodia	S.M. di Licodia	S.M. di Licodia	Valcorrente	Motta S. Anastasia	Motta S. Anastasia	Motta S. Anastasia	Motta S. Anastasia	Motta S. Anastasia	Motta S. Anastasia
SiO_2	46.8	46.6	48.8	49.5	48.8	48.8	48.8	48.7	51.0	51.1	51.1	51.3	51.5	51.5	51.6	50.3	50.4	50.7
TiO_2	1.73	1.74	1.55	1.67	1.59	1.59	1.59	1.53	1.58	1.53	1.56	1.72	1.82	1.83	1.81	1.68	1.68	1.60
Al_2O_3	13.1	13.1	15.3	14.8	14.7	15.1	15.2	15.3	15.7	15.8	15.9	14.8	15.5	15.3	15.7	14.7	14.6	14.8
FeOtot	10.5	10.6	10.9	11.2	11.2	11.1	11.0	10.8	11.1	10.9	10.9	11.6	10.0	10.1	9.94	9.84	9.92	9.82
MnO	0.15	0.15	0.17	0.17	0.18	0.17	0.17	0.17	0.17	0.17	0.17	0.19	0.15	0.16	0.15	0.15	0.16	0.15
MgO	9.43	9.86	7.96	7.44	8.40	7.72	7.77	7.76	5.37	5.30	5.25	5.80	5.16	5.20	4.92	6.47	6.74	6.33
CaO	9.66	9.51	9.95	9.65	9.76	10.1	10.1	10.2	9.70	9.71	9.75	9.67	9.75	9.67	9.59	9.11	9.18	9.40
Na_2O	2.37	2.28	3.28	3.30	3.18	3.32	3.35	3.39	3.47	3.52	3.49	3.12	3.32	3.29	3.31	3.05	3.02	3.23
K_2O	0.31	0.30	0.34	0.41	0.34	0.40	0.39	0.38	0.28	0.28	0.29	0.18	0.71	0.69	0.70	0.63	0.61	0.63
P_2O_5	0.21	0.21	0.35	0.37	0.34	0.35	0.33	0.33	0.25	0.25	0.25	0.21	0.36	0.35	0.35	0.34	0.33	0.34
L.O.I.	5.70	5.63	1.36	1.39	1.40	1.37	1.36	1.46	1.37	1.35	1.35	1.50	1.71	1.91	1.95	3.76	3.40	2.81
Mg#	61.5	62.5	56.5	54.4	57.3	55.6	55.9	56.3	46.5	46.6	46.3	47.3	48.0	48.0	47.1	54.1	54.9	53.6

parallel to the longest side and crosscutting the center of olivine, maintaining a constant spacing between individual spots of 4 μm.

3. Petrological characteristics of the Etnean tholeiites

The volcanic rocks analyzed in this study can be classified as tholeiitic basalts according to the Total Alkali vs. Silica diagram (Le Maitre, 2002; Fig. 3). All rocks show similar $Na_2O + K_2O$ concentrations (2.6–4.0 wt%) at variable SiO_2 content (46.6–51.6 wt%), forming a nearly horizontal trend in the field of basalts. Major element concentrations match those provided in literature for other Etnean tholeiitic basalts, revealing large differences in MgO and other major elements between the Aci Trezza and Adrano Synthem basalts, as well as between individual rock units within the Adrano Synthem (Cristofolini, 1971, 1972, 1973, 1974; Cristofolini et al., 1981; Corsaro and Cristofolini, 1997). The Aci Trezza compositions appear chemically homogeneous. They mostly differ from the Adrano Synthem basalts by higher MgO (9–11 wt% vs 4–8 wt%) and Mg# [100 x Mg/(Mg + Fe) on molar basis, where Fe is expressed as FeO_{tot}] 62–63. Other differences regard the lower Al_2O_3 (12–13 wt% vs. 15–16 wt%), lower Na_2O (~2 wt% vs. 3 wt %) and higher CaO/Al_2O_3 ratio (~0.7 vs. 0.6) in comparison with the composition of the Adrano Synthem group (Table 1). When MgO is used as differentiation index and plotted against major element oxides, it correlates positively with CaO/Al_2O_3 and negatively with SiO_2 and K_2O. The concentration of other oxides remains fairly constant at increasing MgO (Fig. 4). Within the Adrano Synthem rocks, the largest compositional variations are observed in K_2O and FeO_{tot} (Table 1, Fig. 4). The Adrano (ADR) and Biancavilla (BNC) lavas show quite homogeneous chemical features, with compositions that are clustered at the highest MgO (7.4–8.4 wt%). The compositions of Motta Sant'Anastasia (NECK), Valcorrente (VAL) and S. Maria di Licodia (SML) line up in sequence for decreasing MgO values, down to 5.2 wt%. NECK samples appear markedly depleted in FeO_{tot} and enriched in K_2O compared to the other products of the Adrano Synthem suite (Fig. 4).

The Aci Trezza Synthem basalts show variable rock textures and phenocryst associations. The phenocryst content is in the range ~ 5–15 vol%. The phenocryst assemblage includes plagioclase ($An_{60–70}$), olivine ($Fo_{74–86}$) and clinopyroxene ($Wo_{42–45}$-$En_{36–46}$-$Fs_{10–16}$) in variable proportions, where olivine is dominant (see Supplementary Material 1). Plagioclase and olivine are present as individual crystals <1.5 mm in size, rarely exceeding this threshold. The largest olivine and plagioclase phenocrysts are usually anhedral with evidence of resorption. Resorbed olivine displays iddingsite alteration, while the euhedral olivine is typically <0.5 mm in size. Clinopyroxene occurs either as anhedral micro-phenocrysts (~0.5 mm in size) of dominant augitic composition

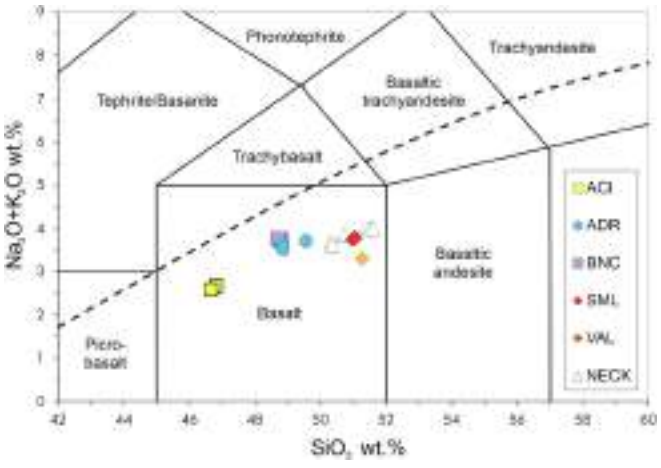

Fig. 3. Classification of the Etnean tholeiites in the Total Alkali vs. Silica diagram (Le Maitre, 2002).

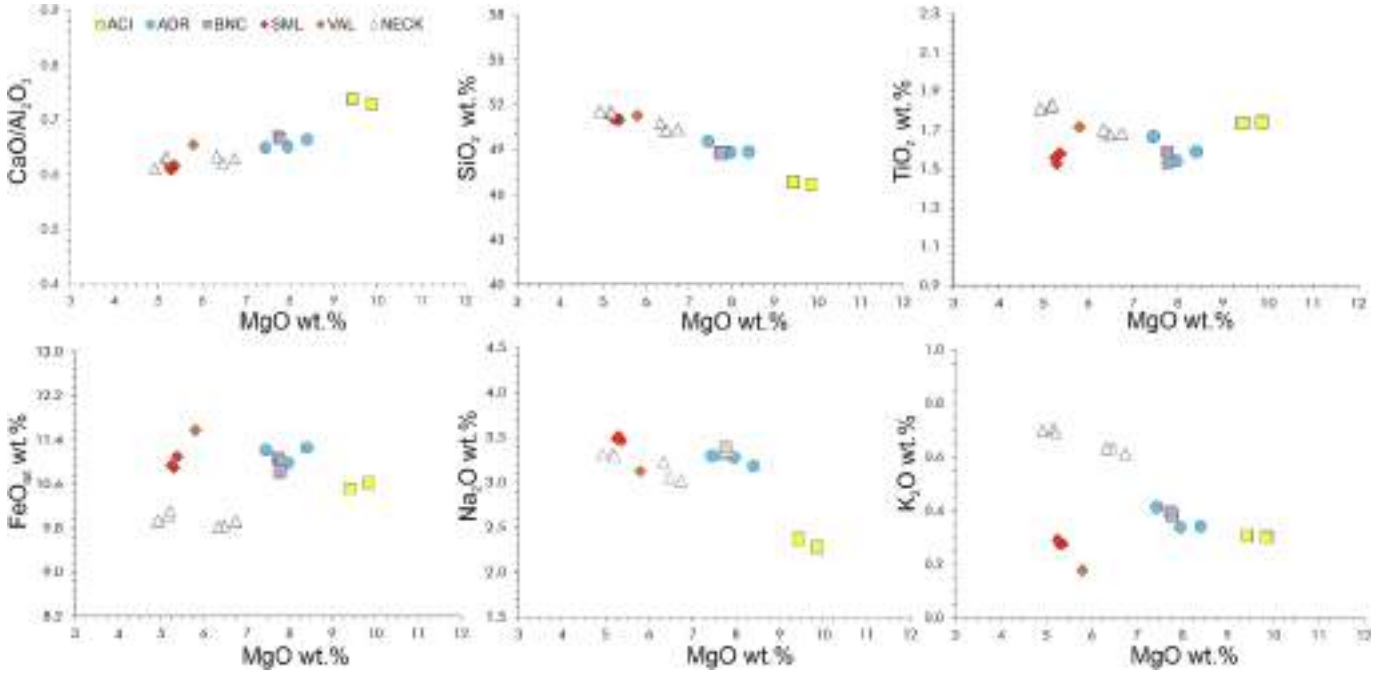

Fig. 4. Plot of MgO vs. major oxides (wt%) for Etnean volcanic rocks belonging to the Aci Trezza and Adrano Synthems.

or as large diopsidic grains (2–4 mm in size), anhedral in shape, and surrounded by plagioclase laths of various sizes, typically <0.4 mm. Rare orthopyroxene phenocrysts (Wo_{3-5}-En_{60-79}-Fs_{17-36}) are also found in some samples. In addition, the mineral assemblage includes abundant Cr and Fe—Ti oxides. Cr oxides are found only enclosed in olivine, showing size up to 50 μm. The groundmass texture varies from vitrophyric to intersertal, mostly composed of small acicular plagioclase microlites.

The petrography of the Adrano Synthem rock suite shows similarities among the ADR, BNC, SML and VAL lavas. These samples display higher phenocryst content (15–25 vol%) than rocks of the Aci Trezza Synthem, and modest differences in rock texture and relative proportions of the phenocryst phases. The phenocryst assemblage is almost entirely composed of euhedral to subhedral olivine (Fo_{58-85}) and plagioclase (An_{47-66}), while clinopyroxene (Wo_{31-43}-En_{35-50}-Fs_{10-24}) is rarely observed. Phenocrysts occur in an intersertal groundmass characterized by a dense network of acicular plagioclase microlites of euhedral shape, with abundant interstitial clinopyroxene, minor olivine, and Fe—Ti oxides. Small Cr-oxides are also present as inclusions in olivine. Within this group of rocks, VAL has the lowest phenocryst content of ~15 vol%, which is mostly composed of olivine, whereas the BNC lavas distinguish for the higher abundance of plagioclase with respect to olivine and the highest phenocryst content (~25 vol%). Unlike the other lavas, BNC contains large (>2 mm) plagioclase crystals affected by resorption and characterized by pervasive sieve textures either at the core or rim.

NECK rocks preserve a subaphyric texture (phenocryst content ~5 vol%) characterized by olivine (Fo_{53-81}) and clinopyroxene (Wo_{31-42}-En_{41-49}-Fs_{11-22}) phenocrysts embedded in a groundmass made of abundant plagioclase and olivine, with clinopyroxene in minor proportion. The size of the phenocryst phases never exceeds 1 mm.

4. Olivine chemistry and zoning profiles

Olivine crystals of the Aci Trezza Synthem suite all display similar core compositions and zoning profiles. The inner cores are characterized by almost flat Fo concentration profiles with compositions within the range Fo_{83-86} (Fig. 5). Rims are normally zoned with decreasing Fo content to Fo_{79-80} or Fo_{74}. Hereafter, we refer to this simple normal zoning profile as to Type 1 (Fig. 6). Two olivine profiles show limited core-to-rim variations in Fo (ΔFo ≤1%) and are therefore considered unzoned (see Supplementary Material 2).

The compositional variability of olivine within the Adrano Synthem suite is quite large. Considering the distribution of core compositions, olivine crystals have been grouped in four main compositional ranges, namely Fo_{83-86}, Fo_{78-81}, Fo_{73-74}, and Fo_{64-70}. The ADR, BNC and VAL lavas contain almost exclusively olivines with Fo_{83-86} cores. More mafic compositions are rare in these samples, or they totally lack (e.g., in BNC; Fig. 5; Supplementary Material 2). Cores at low Fo content (≤Fo_{74}) are only found in NECK and SML. In particular, the NECK olivine compositions fall in three distinct compositional ranges, Fo_{64-70}, Fo_{73-74}, and Fo_{78-81} (Fig. 5; Supplementary Material 2), but Fo_{73-74} cores are by far the most abundant. Aside the four main core groups, we also identified a group of Fo_{82} that is present only in the SML lavas and represents the most mafic olivine composition of these products (Fig. 5; Supplementary Material 2). Fo variations from core to rim form a variety of zoning patterns. The largest group of olivines displays Type 1 zoning (46% of the Adrano Synthem crystals; Fig. 6a-b). Type 1 is present in all lava units of the Adrano Synthem suite, showing Fo gradients that end at various rim compositions from Fo_{53} to Fo_{79}. A second, quite large group of olivines (25% of the crystals) is characterized by normal zoning profiles shifting to smoother or flat profiles at the crystal edge, hereafter Type 2 (Fig. 6a-c). In few instances (10%), we observed profiles similar to the Type 2 that end with a small reverse zoning pattern at the olivine edge, hereafter Type 3 (Fig. 6a-d). Type 2 and Type 3 olivines are abundant within BNC, ADR and SML rocks, though rare examples also exist in NECK. In these profiles, the normal zoning patterns typically re-equilibrate at the compositional range Fo_{63-69}, with a few exceptions at Fo_{79-80} and Fo_{73-74}. In addition to the types described above, we document some step-like Fo profiles (7%), named Type 4, formed by a sequence of two normal zoning patterns connected through a flatter zone at rather constant Fo (Fig. 6a-e). The compositions in these Fo-flat intermediate zones typically oscillate in the range Fo_{78-80}, thus overlapping one of the compositional ranges observed at the core of some crystals or at the rim of Type 2 olivines. We found Type 4 olivines in BNC, ADR and VAL. Finally, at least one olivine per lava unit shows a more complex profile given by the combination of normal plus reverse zoning, hereafter Type 5 (Fig. 6a-f), which overall represents ~12% of the Adrano Synthem olivine suite. Reverse zoning in these crystals

implies that Fo increases by 3–5 mol%, with a maximum at Fo_{85}. It is worth to note that there is not a clear correlation between the composition observed at the core and the occurrence of a specific type of zoning profile.

5. Discussion

5.1. Magma differentiation and crystallization environments

Rock compositions described in this study confirm differences in the evolutionary degree between the oldest Aci Trezza Synthem samples and the more recent Adrano Synthem products. From a mineralogical and geochemical point of view, the ACI samples preserve several features indicating their origin from a magma that underwent very little differentiation. These rocks have the lowest phenocryst content of the Etnean tholeiites, mostly composed of high forsteritic ($Fo_{83–86}$) olivines enclosing numerous grains of Cr-spinel. They also display a narrow range of major oxides compositions at the highest MgO content (~10 wt %) and CaO/Al_2O_3 ratio, with Mg# of 62–63 (Tanguy et al., 1997). By contrast, the Adrano Synthem rock compositions distribute at lower MgO (4–8 wt%) and Mg# (46–57), forming a continuous trend at decreasing MgO and CaO/Al_2O_3 but increasing SiO_2, which suggests that the melt became progressively more differentiated over time, while developing a slightly more alkalic composition. Collectively, all these features suggest that the ACI magma composition could be reasonably assumed as similar to the parent melt from which the Adrano Synthem basalts originated through relatively simple processes of fractional crystallization. On the other hand, the selective removal of diopsidic clinopyroxene and plagioclase over differentiation might explain the large fluctuation in CaO and FeO of these products.

Olivine crystallization and fractionation likely played a dominant role in controlling the chemical evolution of the tholeiitic basalts. The role of olivine is evident from the large variation in the whole-rock MgO (4.9 to 10.6 wt%) and the presence of abundant normally zoned olivine phenocrysts displaying up to 25 mol% of forsterite variation from core to rim. We have evaluated the olivine-melt equilibrium relations by plotting the whole-rock Mg# versus the Fo content in olivine (Fig. 7). In this plot, the equilibrium field is constrained for basaltic melt at Fe/Mg exchange partition coefficient $^{Fe/Mg}K_d = 0.33 \pm 0.04$ (Putirka, 2016). According to this exchange reaction, the equilibrium crystallization with the host rock is attained for mafic olivine populations of ACI samples at high bulk Mg# 62–63 (Fig. 7), whereas olivine compositions from ADR and BNC lavas are close to the equilibrium. The SML and VAL crystals have compositions comparable to the ACI, ADR and BNC cores, but plot above the equilibrium field to the left of the diagram. Their high Fo content at the lowest Mg# indicates an origin within a melt more mafic than that feeding the growth of olivine, and also suggests that olivine

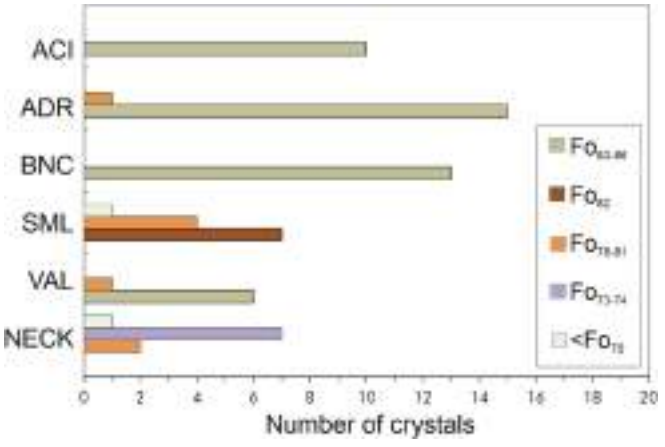

Fig. 5. Distribution of forsterite in olivine cores from the Etnean tholeiites.

removal was the process controlling the mineral-melt disequilibrium in relation to the Fe—Mg exchange. Samples below the equilibrium field have probably experienced differentiation and olivine removal based on the low Fo contents of olivine crystals and the associated whole-rock Mg#. In this context, the NECK crystals display more complex equilibrium relations, with one group of olivines that fall in or just out of the equilibrium field and one olivine plotting well below the equilibrium, which can be considered as a late crystallizing grain.

The compositional variability of the studied olivines is not much different from that of the recent volcanic products, given the occurrence of core compositions and zoned profiles similar to those documented since 1991 (e.g., Kahl et al., 2013, 2015; Giuffrida and Viccaro, 2017; Cannata et al., 2018; Viccaro et al., 2019; Borzì et al., 2020; Giuffrida et al., 2021, 2023). However, the compositional differences between crystals of the Aci Trezza and the Adrano Synthem rock suites suggest contrasting histories of storage and transport during these two periods of volcanic activity. For instance, the chemical homogeneity of the ACI olivine phenocrysts, all showing Type 1 or nearly flat profiles at $Fo_{83–86}$ composition, supports the idea that conditions of magma storage and crystallization were quite uniform during the earliest stage of Etnean magmatism. The Fo content in olivine is an effective recorder of the composition of the melt that carries the crystal from source to surface because of the high sensitivity to melt chemistry changes due to crystallization and mixing processes (cf. Kahl et al., 2015; Chakraborty and Dohmen, 2022). The nearly constant Fo concentrations measured at the olivine core can be therefore considered a reflection of the composition of the initial magma batch in which the olivine starts to form, while the composition of the final host magma would be represented by the crystal rim composition. Hence, the ACI olivine crystals must have spent the majority of their existence in a mafic, compositionally and physically homogeneous environment to develop nearly flat, 100–250 μm-long core profiles in equilibrium with the host melt composition (see Supplementary Material 2). Later, these flat profiles may evolve in Type 1 normal zoning during the crystal transfer from storage conditions to eruption, ensuing melt chemistry change. The absence of evident zoning in some crystals was likely the effect of the rapid ascent and emission of the magma batch carrying the olivine rather than diffusive re-equilibration of the Fe—Mg component, in accordance with the olivine-equilibrium relations and the low degree of groundmass crystallization of these products.

The Adrano Synthem olivine crystals depict a different scenario of magma evolution in which more than one single storage zone can be identified. Four distinct olivine populations were defined based on the Fo core distributions, $Fo_{83–86}$, $Fo_{78–81}$, $Fo_{73–75}$, and $Fo_{64–70}$. These populations realistically reproduce the magmatic composition of mineral saturation and can be linked to distinct crystallization zones in the magma plumbing system (cf. Kahl et al., 2015; Chakraborty and Dohmen, 2022). Several crystals display growth zones at nearly constant Fo composition at the core and rim (e.g., Type 2 and Type 4), which suggest chemical re-equilibration of the olivine at magmatic conditions different than those of the core formation before eruption. However, the distribution of olivine core populations and zoning type is not homogeneous between the distinct rock units of the Adrano Synthem suite. As the majority of core compositions are $Fo_{83–86}$, it is conceivable that a common primitive magmatic environment of crystallization existed, and this environment must have fed the different eruptions of that time. Nevertheless, the occurrence of minor core populations and the heterogeneity of zoning profiles indicate that the magmatic conditions of crystal residence and transport have changed during the Adrano Synthem volcanic phase.

The analysis of compositional variations in magmatic crystals alone is unfortunately neither sufficient to establish the existence of discrete magmatic storage regions nor it can be used to determine how the storage and transfer conditions changed over time. Using crystals and whole-rock data from this study, we applied thermodynamic calculations by the rhyolite-MELTS code v. 1.2.0 (Ghiorso and Sack, 1995;

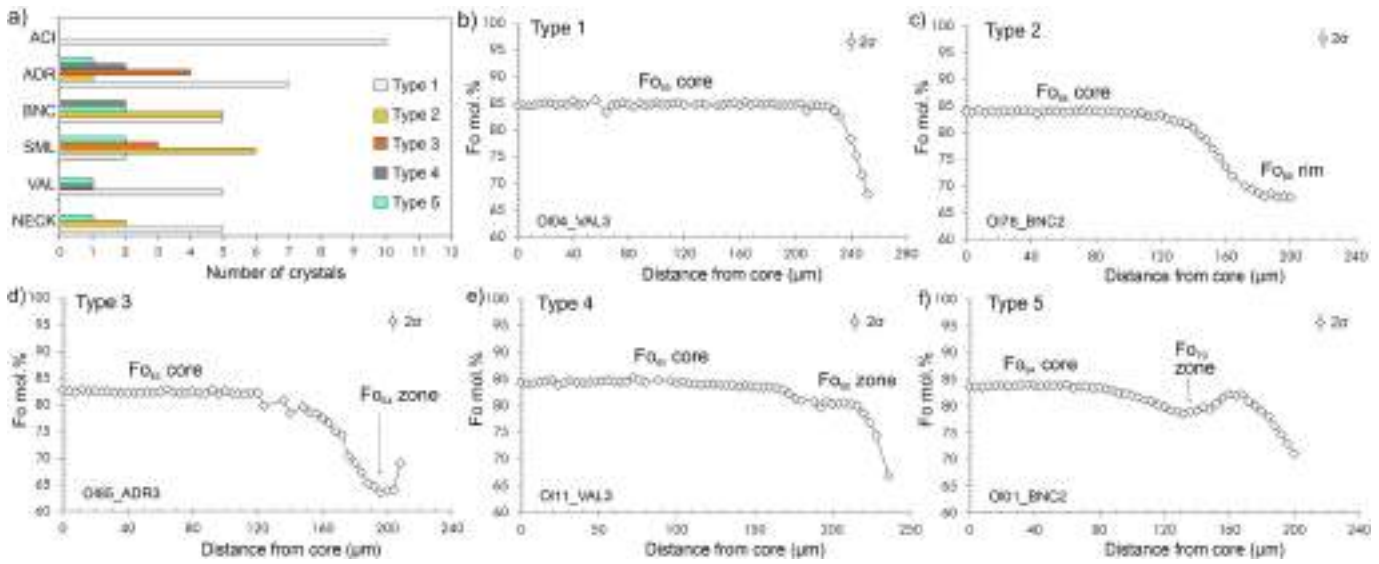

Fig. 6. Types of olivine zoning and distribution between the volcanic rock units of this study. Fo mol.% = Forsterite mol.% calculated as 100 × [Mg/(Mg + Fe + Mn)] on molar basis, where iron is expressed as FeO_{tot}. The 2σ error bars are shown in each plot.

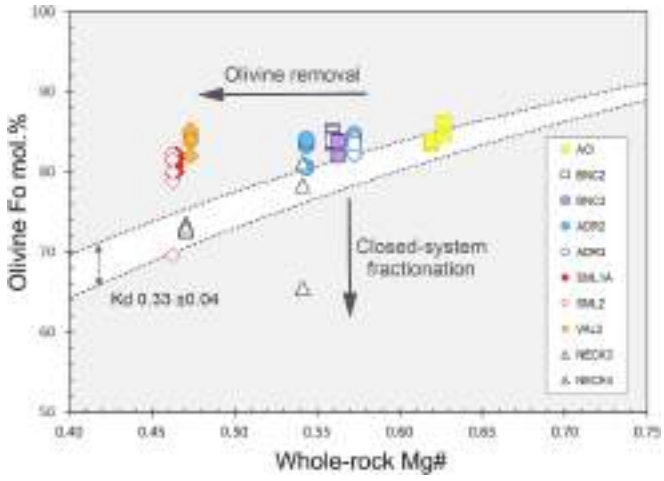

Fig. 7. - Mg# [100 × Mg/(Mg + Fe) on molar basis, where Fe is expressed as FeO_{tot}] of whole-rock plotted against the forsterite content (Fo mol.%) of olivine cores from the Etnean tholeiites. The diagonal white field is the shallow pressure (1 atm) equilibrium field for basaltic magma ($^{Fe/Mg}K_d = 0.33 \pm 0.04$; Putirka, 2016).

Gualda et al., 2012; Ghiorso and Gualda, 2015) to simulate magma evolution and define the set of chemical and physical variables (*X*, T, P, fO_2) under which distinct mineral populations formed. The initial composition representative of the primary liquid was obtained through the PRIMELT3 MEGA.XLSM algorithm (Herzberg and Asimow, 2015) that provides a mass balance-like solution based on the addition of olivine to a basic lava to recover the composition of the primary melt. As input data to PRIMELT3, we used the bulk rock composition of the ACI1b sample, being the most mafic among the studied rocks (SiO_2 = 46.6 wt%, MgO = 9.86 wt%; Mg# = 63; Table 1). The output primary composition in equilibrium with Fo_{92} olivine was then used as initial liquid phase to start calculations (Supplementary Material 3). Thermodynamic rhyolite-MELTS runs were conducted under both crystal and fluid fractionation to simulate crystallization from the mantle-crust boundary at 20–25 km b.s.l. (Cristofolini et al., 1985) upward to the surface. Simulations were performed along different fO_2 paths, including the Nickel-Nickel Oxide (NNO) and the Quartz-Fayalite-Magnetite (QFM-1 to QFM + 1) oxygen buffers and variable melt volatile budgets (initial H_2O from ca. 6.0 to 0.5 wt% and CO_2 from ca. 6000 to 200 ppm). These ranges cover the wide spectrum of crystallization conditions estimated for Etnean magmas, as determined by melt inclusions (e.g., Métrich et al., 2004; Spilliaert et al., 2006; Kamenetsky et al., 2007; Collins et al., 2009; Gennaro et al., 2019; Zuccarello et al., 2021, 2022). Target of the modeling was to obtain the whole spectrum of olivine observed, as well as a mineral assemblage consistent with that of the natural samples. The modeling was also aimed at producing a liquid line of descent that replicates at the best the whole-rock geochemical trends, i.e. matching well the variations in major oxides during differentiation. This assumption can be acceptable in light of the marked mafic character and low porphyricity of the studied samples.

The best simulation matching all the above-mentioned criteria for the Etnean tholeiites was obtained at the following physical and chemical conditions: pressure 600–25 MPa; temperature 1310–1080 °C; initial H_2O = 3 wt%; initial CO_2 = 600 ppm; fO_2 at the QFM buffer (Fig. 8; see also Supplementary Material 3). Despite the overall good fit, the liquid line of descent shows MgO depletion and TiO_2 plus Al_2O_3 enrichment with respect to the compositions of the most evolved rocks of the Adrano Synthem period. This discrepancy suggests late crystallization of spinel and Fe-Ti-oxides and limited fractionation of olivine in the modeled liquid line of descent compared to the natural conditions, especially in the late stages of magma differentiation. Fo_{89} olivine is the first crystallizing mineral phase at 1310 °C, followed by augitic clinopyroxene, spinel and Ca-rich plagioclase as the magma progressively cools. The simulation reproduced various populations of olivine forming under different *X-P-T-*fO_2 conditions. The modeled *P-T* ranges for distinct crystal populations were then used to calculate the buffering conditions of the system according to the model of Kress and Carmichael (1991). Results are synthetized in the Supplementary Material 3. The largest and most basic population observed for the Etnean tholeiites (i.e. $Fo_{83–86}$ olivine) crystallizes at 380–230 MPa, 1220–1160 °C and oxygen fugacity ($\log fO_2$) values between −8.2 and − 8.6. The thermodynamic variables allowing the crystallization of the olivine at $Fo_{78–81}$ include magmatic pressure and temperature of 160–100 MPa and 1135–1110 °C and $\log fO_2$ between −9.0 and − 9.4. Fo_{82} olivines (only found in the SML basalts) occur at ~180–200 MPa and 1140–1150 °C. During differentiation from 380 MPa and 1220 °C down to 100 MPa and 1110 °C, olivine is the only crystallizing and fractionating mineral phase. The melt experiences low degree of crystallization (total solid fraction of ~5%), which results into limited variations in H_2O (4.6–3.0 wt%) and CO_2 (830–740 ppm).

The $Fo_{73–74}$ and $\leq Fo_{70}$ core populations form at very shallow levels, after ~2 wt% H_2O is lost through degassing. $Fo_{73–74}$ olivines are reproduced at ~40 MPa, 1090 °C and logfO_2 close to −9.7, whereas $\leq Fo_{70}$ olivine core compositions can be only obtained below 25 MPa and 1080 °C, at log$fO_2 \leq -9.8$. Under these thermodynamic conditions, the olivine coexists with augitic clinopyroxene and Ca-poor plagioclase with composition $An_{79–71}$, close to those found in natural rock samples. Opaque oxides only crystallize at the latest stage of melt differentiation at temperature lower than 1080 °C. For simplicity, we named the environments representative of the four different olivine core populations as M1 ($Fo_{83–86}$), M2 ($Fo_{78–81}$), M3 ($Fo_{73–75}$) and M4 ($Fo_{64–70}$) from the most primitive to the most evolved compositions. The proximity of conditions that define the environments M3 and M4 suggests that these environments could be part of a single shallow storage region (e.g., a zoned reservoir), rather than different physical storage regions.

If each olivine core population defines a specific magmatic environment of crystal growth, then the frequency of these populations in natural samples can be the proxy of the frequency by which individual magmatic environments were activated during discrete periods of volcanic activity. On the other hand, the type of zoning profile reflects the entire crystal growth history and can be used to infer the sequence of environments an olivine has passed through before eruption (Costa et al., 2020; Chakraborty and Dohmen, 2022). In this regard, the Type 1 zoning can be considered as a marker of crystal migration from the

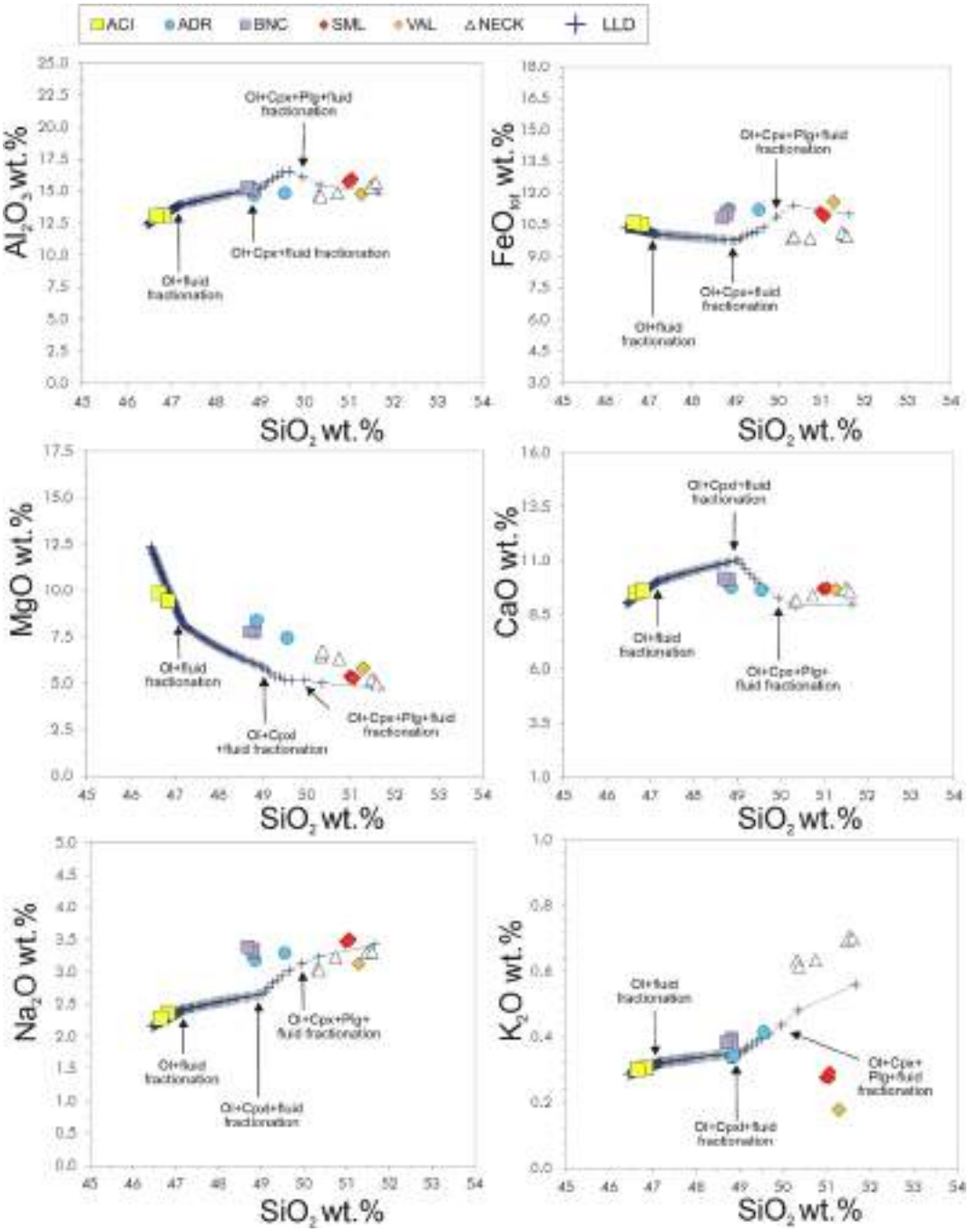
ACI
ADR
BNC
SML
VAL
NECK
LLD
Al2O3 wt.%
FeOtot wt.%
MgO wt.%
CaO wt.%
Na2O wt.%
K2O wt.%
SiO2 wt.%
Ol+Cpx+Plg+fluid fractionation
Ol+Cpx+fluid fractionation
Ol+fluid fractionation
Ol+Cpx+fluid fractionation
Ol+Cpx+Plg+fluid fractionation
Ol+Cpx+Plg+ fluid fractionation
Ol+Cpx+Plg+ fluid fractionation
Ol+Cpx+ Plg+fluid fractionation
Ol+Cpx+Plg+ fluid fractionation
Ol+Cpx+Plg+ fluid fractionation
Ol+Cpx+Plg+

initial storage region to the surface due to the absence of Fo-flat zone at the rim. Similar zoning types could alternatively be produced during residence at high fO_2, a condition that prevents the growth of olivine, while favoring the crystallization of plagioclase and clinopyroxene. This interpretation, however, does not match the petrological characteristics of the Aci Trezza basalts, because the phenocryst content of these rocks is dominated only by Type 1 olivines with very limited plagioclase and clinopyroxene. The Aci Trezza Synthem basalts exclusively record such direct migration paths starting from a mafic storage region located at 380–250 MPa and represented by the M1 magma. The Type 2 zoning, where flat zones occur both at the core and edge linked by normal zoning pattern, is the best marker of olivine transport from an initial crystallization environment (represented by core composition) to a final more evolved environment of residence (the rim composition), where the crystal experiences a further stage of growth under rather stable physical and chemical conditions. Type 2 is common in ADR, BNC and SML. The compositional variation of the Type 2 profiles in the ADR and BNC rocks typically indicates olivine transfer from M1 to M4, while the dominant path in SML implies migration from an environment intermediate between M1 and M_2 (at Fo_{82}) to M4 (Figs. 6 and 9). However, some profiles account for olivine chemical re-equilibration at the condition of M2 and M3 as well. Their presence suggests more complex ascent pathways for magmas feeding the ADR, BNC and SML lavas, implying that magmas passed through at least three physically and chemically distinct storage regions. The analysis of the VAL olivines reveals more direct migration paths to the surface, where only the most mafic M1 and M2 environments were involved. No further steps of olivine residence in the shallower environments are evident based on Fo zoning.

We have interpreted the abundance of low-Fo cores in the NECK samples as the natural consequence of the emplacement and slow, nearly isothermal solidification of the Motta Sant'Anastasia volcanic neck at shallow depth. The remobilization of the M2 magma from a storage region at ~170–100 MPa may have been the driving process for magma intrusion and emplacement at low pressure. This assumption derives from the observation of $Fo_{78–81}$ crystals with Type 2 zoned rims that are re-equilibrated at low Fo in the range Fo_{64} to Fo_{66}.

5.2. Timescales of magmatic processes

Whilst the distinct zoning profiles are indicative of a range of pre-eruptive processes of magmatic storage and migration, the re-equilibration of olivine compositional gradients via chemical diffusion indirectly provides the durations of these processes within magma storage regions before eruption. Timescales were calculated for Fe—Mg interdiffusion in 38 zoned olivine crystals (see Supplementary Material 4).

Chemical profiles were modeled numerically with the method of finite difference (Costa et al., 2008; Costa and Morgan, 2010) applying concentration-dependent diffusion coefficients [$D_{Fe\text{-}Mg}$; Dohmen and Chakraborty, 2007] and the crystal rim composition as boundary condition. Step-like concentration profiles were used as initial distribution to model most of the zoned olivines. This choice follows the assumption that diffusion starts as the crystal is incorporated in a magmatic environment having quite different thermodynamic characteristics than the initial host environment, a condition that causes abrupt compositional changes in the crystal itself. In Type 1 olivine, we considered an initial homogeneous distribution to start the modeling, which is in accordance with the assumption that diffusion is driven by later change of concentrations at the crystal boundary due to the final event of magma ascent (Costa and Chakraborty, 2004).

The diffusivity for Fe—Mg in olivine is governed by changes in temperature and oxygen fugacity, as well as in pressure (Dohmen and Chakraborty, 2007; Dohmen et al., 2007; Chakraborty, 2010; Costa and Morgan, 2010). Therefore, the Fe—Mg diffusion coefficients were calculated by using the set of thermodynamic parameters (T, P, and fO_2) defining the magmatic environment where the olivine re-equilibrates before eruption, in accordance with thermodynamic modeling results. By modeling chemical profiles at the higher re-equilibration temperature within the estimated range, we ascertain a minimum time since the onset of diffusion. The effects of crystallographic orientation have been also incorporated in the calculation of $D_{Fe\text{-}Mg}$ (Dohmen and Chakraborty, 2007; Dohmen et al., 2007; Costa et al., 2008; Chakraborty, 2010; Costa and Morgan, 2010). We accounted for diffusion anisotropy by determining the angles between olivine a-, b- and c- crystallographic axes and the SEM-EDS/WDS traverses. Crystallographic axes were measured by conoscopic observations under a polarizing optical microscope equipped with a Zeiss 4 axis universal stage. The α, β and γ angles between the analytical traverse and the crystallographic axes of the olivine were finally used to calculate Fe—Mg diffusion coefficient parallel to the traverse direction in which composition is measured (Dohmen and Chakraborty, 2007). Concentration profiles obtained from randomly sectioned olivine crystals were not modeled. Typically, the largest errors result from modeling profiles in sections that are oblique to crystal faces. Off-center sections intersect crystal faces at very different angles, thus generating apparent concentration gradients of

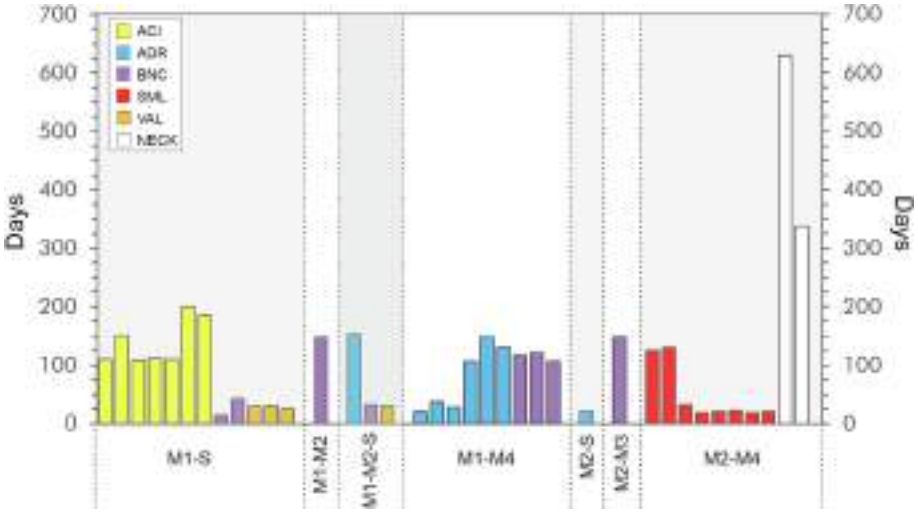

Fig. 9. Timescales (in days) distributions calculated for the residence and transfer of olivine crystals between magmatic environments (M*i*) in different periods of the Aci Trezza and Adrano Synthems.

different widths (Wallace and Bergantz, 2003; Shea et al., 2015a, 2015b). To avoid sectioning effects, among the numerous olivines exposed in thin sections, we have selected only olivine sections cutting the crystal close to the fastest diffusion direction (i.e., the c-axis; Costa and Chakraborty, 2004). Moreover, we disregard the smallest olivines, which have high probability of being off-center sections of olivine (Shea et al., 2015a, 2015b). All timescales were obtained under the assumption that concentration profiles originated by diffusion only. The potential effect of crystal growth/dissolution on the final timescales has been not resolved because of the low analytical resolution obtained by SEM-EDS/WDS for minor elements diffusing at different rates (Shea et al., 2015a, 2015b; Oeser et al., 2018). Assuming a diffusion-only contribution, the model produces longer timescales than those resulting from concentration profiles affected by processes other than diffusion (Costa et al., 2008). Despite these limitations, a diffusion-only approach is effective when it comes to highlighting relative differences in timescales between magmatic processes characterizing distinct periods of volcanic activity.

Uncertainties on diffusion timescales were obtained by propagating the error in the determination of diffusion coefficients, following the criteria introduced by Kahl et al. (2015). The procedure accounts for uncertainties of ±10 °C in temperature and ± 0.25 logfO_2 on the thermodynamic conditions of crystallization of different olivine populations. Timescales and associated uncertainties for the entire olivine dataset are reported in Table 2.

Most of the modeled crystals exhibit one simple normal zoning pattern (e.g., Type 1, Type 2 and Type 3) and were therefore modeled at isothermal conditions, accounting for olivine chemical relaxation at the temperature of the final host environment. For crystals with more complex zoning profiles (e.g., Type 4 and Type 5), the diffusion modeling was performed non isothermally in multiple steps, assuming different re-equilibration temperatures for the interior zone and for the rim zone based on the sequence of zoning patterns, normal or reverse. Chemical gradients too small (~1 Fo mol.%) or too short (formed by just few analytical spots) were not modeled. All the compositional traverses in olivine crystals of distinct lava units and the associated diffusion curves obtained by modeling the Fe—Mg diffusion are available in the Supplementary Material 4, whereas the distribution of timescales in different rock units is illustrated in Fig. 9.

The majority of the crystals defines two clusters of timescales ranging from 18 to 46 days ($n = 19$) and 106–200 days ($n = 18$), respectively. Timescales obtained for the ACI crystals vary in the range 109–200 days and all refer to the olivine transfer from the deepest storage region at ~380 MPa (M1 environment) directly to the surface. Timescales for ADR, BNC and SML olivines span a much wider range from 18 to 185 days. Most of these timescales relates to multi-stage traveling along the dominant pathway M1-M4 for the ADR and BNC crystals, and the pathway M2-M4 for the SML crystals. Crystals that followed these paths record either short (≤46 days) or significantly longer timescales (≥106 days), suggesting the control of processes that facilitate or prevent magma supply during the volcanic activity. Despite the compositional similarities, we obtained somewhat longer timescales from the BNC olivines compared to ADR and SML (Fig. 9; Supplementary Material 3). Timescales, however, appear in accordance with the observed

Table 2
Fe—Mg diffusion timescales (in days) and relative uncertainties (±σ) for olivine crystals of the Aci Trezza Synthem and the Adrano Synthem. The modeled zoning patterns (n: normal; r: reverse) and the associated connections between magmatic environments (M_i) are shown for different types of zoned crystals. The sequence of *T-P-fO₂* values in complex zoned olivines refers to the thermodynamic parameters used for modeling distinct zoned portions of a crystal.

Rock sample	Olivine	Zoning type	T (°C)	P (MPa)	LogfO_2	Connected environments	Δt ± σ
ACI2	Ol9_ACI2	1	1135	180	−9.02	M1-S (n)	110 ± 50
ACI2	Ol12_ACI2	1	1135	180	−9.02	M1-S (n)	200 ± 92
ACI2	O25_ACI2	1	1135	180	−9.02	M1-S (n)	151 ± 72
ACI2	Ol4_ACI2	1	1135	180	−9.02	M1-S (n)	110 ± 50
ACI2	Ol1_ACI2	1	1090	40	−9.67	M1-S (n)	109 ± 50
ACI2	Ol2_ACI2	1	1090	40	−9.67	M1-S (n)	111 ± 50
BNC2	Ol1_BNC2	5	1135 + 1220 + 1080	180 + 180 + 25	−9.02/−8.41/−9.79	M1-M2-S (n + r + n)	32 ± 14
BNC2	Ol2_BNC2	4	1135 + 1080	180 + 25	−9.02/−9.79	M1-M2-S (n + n)	18 ± 8
BNC2	Ol43_BNC2	2	1135	180	−9.02	M1-M2 (n)	148 ± 66
BNC2	Ol78_BNC2	2	1080	25	−9.79	M1-M4 (n)	116 ± 53
BNC3	Ol99_BNC3	2	1080	25	−9.79	M1-M4 (n)	120 ± 56
BNC3	Ol55_BNC3	2	1080	25	−9.79	M1-M4 (n)	106 ± 50
BNC3	Ol8_BNC3	1	1080	25	−9.79	M1-S (n)	46 ± 20
ADR2	Ol18_ADR2	4	1135 + 1080	180 + 25	−9.02/−9.79	M1-M2-S (n + n)	153 ± 72
ADR2	Ol19_ADR2	1	1080	25	−9.79	M1-S (n)	185 ± 81
ADR2	Ol38_ADR2	1	1080	25	−9.79	M2-S (n)	28 ± 13
ADR2	Ol144_ADR2	2	1080	25	−9.79	M1-M4 (n)	130 ± 62
ADR3	Ol85_ADR3	3	1080	25	−9.79	M1-M4 (n)	106 ± 48
ADR3	Ol09_ADR3	3	1080	25	−9.79	M1-M4 (n)	148 ± 61
ADR3	Ol121_ADR3	2	1080	25	−9.79	M1-M4 (n)	21 ± 9
ADR3	Ol136_ADR3	3	1080	25	−9.79	M1-M4 (n)	37 ± 16
ADR3	Ol143_ADR3	2	1080	25	−9.79	M1-M4 (n)	28 ± 13
SML1A	Ol1_SML1A	2	1080	25	−9.79	M2-M4 (n)	21 ± 10
SML1A	Ol25_SML1A	3	1080	25	−9.79	M2-M4 (n)	19 ± 8
SML1A	Ol54_SML1A	2	1080	25	−9.79	M2-M4 (n)	23 ± 12
SML1A	Ol55_SML1A	2	1080	25	−9.79	M2-M4 (n)	21 ± 11
SML2	Ol08_SML2	3	1080	25	−9.79	M2-M4 (n)	32 ± 16
SML2	Ol02_SML2	3	1080	25	−9.79	M2-M4 (n)	19 ± 9
SML2	Ol05_SML2	2	1080	25	−9.79	M2-M4 (n)	130 ± 62
SML2	Ol12_SML2	2	1080	25	−9.79	M2-M4 (n)	125 ± 60
SML1A	Ol44_SML1A	2	1090	40	−9.67	M2-M3 (n)	148 ± 66
VAL3	Ol5_VAL3	5	1220 + 1135	180	−8.41/−9.02	M1-M2-S (r + n)	30 ± 14
VAL3	Ol11_VAL3	4	1135 + 1080	180 + 25	−9.02/−9.79	M1-M2-S (n + n)	21 ± 10
VAL3	Ol17_VAL3	1	1080	25	−9.79	M1-S (n)	25 ± 10
VAL3	Ol18_VAL3	1	1080	25	−9.79	M1-S (n)	30 ± 14
VAL3	Ol04_VAL3	1	1080	25	−9.79	M1-S (n)	29 ± 14
NECK4	Ol38_NECK4	2	1080	25	−9.79	M2-M4 (n)	343 ± 124
NECK4	Ol39_NECK4	2	1080	25	−9.79	M2-M4 (n)	630 ± 300

petrographic differences between these samples (e.g., higher abundance of plagioclase and disequilibrium plagioclase textures in the BNC rocks), confirming more complex shallow dynamics characterizing the volcanic activity in the area of Biancavilla with respect to the nearby areas. All diffusion profiles of the VAL olivines provide very short timescales of 21–30 days, which account for pre-eruptive storage and transport throughout the M1 and M2 magmatic zones. In our dataset, only two profiles give timescales longer than 340 days. They both belong to the NECK units and indicate prolonged phases of olivine residence and diffusive relaxation at the condition of M4.

6. Evolution of the Etnean embryonic plumbing system

Petrological investigations have revealed one single olivine population within the plumbing system during the Aci Trezza Synthem phase and at least three additional olivine populations during the Adrano Synthem phase. Products erupted during the Aci Trezza Synthem period do not show evidence of interaction between magma volumes with different evolutionary degrees. In this regard, we have not found indications of reverse zoning, which is commonly attributed to magma hybridization processes, in any olivine of the Aci Trezza Synthem. Rather, all crystals record simple migration paths from deep storage regions until the eruption. During the Aci Trezza Synthem phase, primitive magmas therefore intruded into the deep plumbing system at pressure of 250–380 MPa (corresponding to depths of 9–14 km assuming 2.7 g/cm^3 crustal density; Corsaro and Pompilio, 2004), leading to the crystallization of $Fo_{83–86}$ olivine. The calculated range of timescales points out good drainage capability of the plumbing system, as the magma carrying these $Fo_{83–86}$ olivines moved directly upward to the surface over relatively short times. All these characteristics are in accordance with large accumulation of mantle-derived magmas into the deep crust, which were able to pressurize the crust promoting the onset of Etnean volcanism, a feature also coherent with the Late Quaternary uplift rates in eastern Sicily (cf. Catalano et al., 2004). According to these authors, the deep accumulation of magmas generated crustal doming and development of strike-slip tectonics, finally leading to transtensional regimes active until the onset of the alkaline stage of activity at ~130 ka.

The Adrano Synthem lavas share similarities with the Aci Trezza Synthem products because of the systematic occurrence of $Fo_{83–86}$ olivine cores. However, differences occur for either the evolutionary degree of erupted products or the presence of olivine populations and zoning patterns, reflecting dynamics of storage and transfer at shallow depth more complex than those of the Aci Trezza Synthem period. Undoubtedly, such features indicate a common deep reservoir for the Aci Trezza and the Adrano Synthem magmas, but also that during the inferred temporal hiatus of ~200 ka, as during the temporal interval between the emplacement of the submarine and the subaerial volcanic rocks, important changes in the plumbing system configuration occurred. Indeed, crystals from distinct units of the Adrano Synthem have experienced different transport histories from nucleation to eruption, developing compositionally distinct growth zones at various chemical and physical conditions. The widespread presence of nearly flat growth zones at the olivine cores and rims supports the assumption that magma stalled in distinct shallower storage zones within the plumbing system, allowing the diffusive re-equilibration of their olivine cargo during storage. The picture arising from the olivine zoning patterns of the Adrano Synthem phase, along with the general slowing down of storage/transfer processes, emphasize the progressive decline over time of the transtensional tectonic regimes, which culminated at around 130 ka and caused the shift to volcanism dominated by central-type edifices.

CRediT authorship contribution statement

Marisa Giuffrida: Writing – original draft, Visualization, Validation, Methodology, Investigation, Formal analysis, Data curation. **Eugenio Nicotra:** Writing – original draft, Visualization, Formal analysis, Data curation. **Marco Viccaro:** Writing – original draft, Validation, Supervision, Resources, Project administration, Methodology, Investigation, Funding acquisition, Formal analysis, Data curation, Conceptualization.

Declaration of competing interest

The authors declare that they have no known competing financial interests or personal relationships that could have appeared to influence the work reported in this paper.

Data availability

All the data referring to the manuscript have been included in the submission as supplementary online materials

Acknowledgements

This work is dedicated to the memory of Prof. Renato Cristofolini, who was among the first researchers devoting time and efforts in the study of the early volcanic manifestations of Mt. Etna. The study was supported by the funding program PIACERI 2020-22 of the University of Catania, project PAROSSISMA, code 22722132140 (Principal Investigator M. Viccaro). The Authors are also very grateful to the support received by Giancarlo Niceforo for the XRF analyses at the University of Calabria and by Alfio Viola for the SEM-EDS/WDS in situ measurements at the University of Catania. The authors thank Ed Llewellin for the editorial handling of the manuscript and Silvio Mollo and Pavel Izbekov for their constructive comments and suggestions provided during the revision process.

Appendix A. Supplementary data

Supplementary data to this article can be found online at https://doi.org/10.1016/j.jvolgeores.2024.108113.

References

Borzì, A.M., Giuffrida, M., Zuccarello, F., Palano, M., Viccaro, M., 2020. The Christmas 2018 eruption at Mt. Etna: enlightening how the volcano factory works through a multi-parametric inspection. Geochem. Geophys. Geosyst. 21 e2020GC009226.
Branca, S., Del Carlo, P., 2005. Types of eruptions of Etna volcano AD 1670-2003: Implications for short-term eruptive behaviour. Bull. Volcanol. 67, 732–742.
Branca, S., Coltelli, M., Groppelli, G., 2004. Geological evolution of Etna volcano. In: Bonaccorso, A., Calvari, S., Coltelli, M., Del Negro, C., Falsaperla, S. (Eds.), Mt. Etna Volcano Laboratory, AGU Geophysical Monograph Series, vol. 143, pp. 49–63.
Branca, S., Coltelli, M., De Beni, E., Wijbrans, J., 2008. Geological evolution of Mount Etna volcano (Italy) from earliest products until the first central volcanism (between 500 and 100 ka ago) inferred from geochronological and stratigraphic data. Int. J. Earth Sci. 97, 135–152.
Branca, S., Coltelli, M., Groppelli, G., Lentini, F., 2011a. Geological map of Etna volcano, 1:50,000 scale. Ital. J. Geosci. 130, 265–291.
Branca, S., Coltelli, M., Groppelli, G., 2011b. Geological evolution of a complex basaltic volcano: Mount Etna, Italy. Ital. J. Geosci. 130, 306–317.
Cannata, A., Di Grazia, G., Giuffrida, M., Gresta, S., Palano, M., Sciotto, M., Viccaro, M., Zuccarello, F., 2018. Space-time evolution of magma storage and transfer at Mt. Etna volcano (Italy): the 2015-2016 reawakening of Voragine crater. Geochem. Geophys. Geosyst. 19, 471–495.
Catalano, S., Torrisi, S., Ferlito, C., 2004. The relationship between late Quaternary deformation and volcanism of Mt. Etna (eastern Sicily): new evidence from the sedimentary substratum in the Catania region. J. Volcanol. Geotherm. Res. 132, 311–334.
Chakraborty, S., 2010. Diffusion coefficients in olivine, wadsleyite and ringwoodite. Rev. Mineral. Geochem. 72, 603–639.
Chakraborty, S., Dohmen, R., 2022. Diffusion chronometry of volcanic rocks: looking backward and forward. Bull. Volcanol. 84, 1–9.
Clocchiatti, R., Schiano, P., Ottolini, L., Bottazzi, P., 1998. Earlier alkaline and transitional magmatic pulsation of Mt. Etna volcano. Earth Planet. Sci. Lett. 132, 25–41.
Collins, S.J., Pyle, D.M., Maclennan, J., 2009. Melt inclusions track pre-eruption storage and dehydration of magmas at Etna. Geology 37, 571–574.
Corsaro, R.A., Cristofolini, R., 1997. Geology, geochemistry and mineral chemistry of tholeiitic to transitional Etnean magmas. Acta Vulcanol. 9, 55–66.

Corsaro, R.A., Cristofolini, R., 2000. Subaqueous volcanism in the Etnean area: evidence for hydromagmatic activity and regional uplift inferred from the Castle Rock of Acicastello. J. Volcanol. Geotherm. Res. 95, 209–225.
Corsaro, R.A., Pompilio, M., 2004. Buoyancy-controlled eruptions of magmas at Mt. Etna. Terra Nova 16, 6–22.
Corsaro, R.A., Métrich, N., Allard, P., Andronico, D., Miraglia, L., Fourmentraux, C., 2009. The 1974 flank eruption of Mount Etna: an archetype for deep dike-fed eruptions at basaltic volcanoes and a milestone in Etna's recent history. J. Geophys. Res. 114 (7), B07204.
Costa, F., Chakraborty, S., 2004. Decadal time gaps between mafic intrusion and silicic eruption obtained from chemical zoning patterns in olivine. Earth Planet. Sci. Lett. 227, 517–530.
Costa, F., Morgan, D., 2010. Time constraints from chemical equilibrium in magmatic crystals. In: Dosseto, A., Turner, S.P., Van-Orman, J.A. (Eds.), Timescales of Magmatic Processes: From Core to Atmosphere. Wiley-Blackwell, pp. 125–159.
Costa, F., Dohmen, R., Chakraborty, S., 2008. Time scales of magmatic processes from modeling the zoning patterns of crystals. Rev. Mineral. Geochem. 69, 545–594.
Costa, F., Shea, T., Ubide, T., 2020. Diffusion chronometry and the timescales of magmatic processes. Nat. Rev. Earth Environ. 1, 201–214.
Cristofolini, R., 1971. La distribuzione del titanio nelle vulcaniti etnee. Periodico di Mineralogia 1-2, 41–66.
Cristofolini, R., 1972. I basalti a tendenza tholeiitica dell'Etna. Periodico di Mineralogia 1, 167–200.
Cristofolini, R., 1973. Recent trends in the study of Etna. Philos. Trans. R. Soc. Lond. 274, 17–35.
Cristofolini, R., 1974. La massa subvulcanica di Acitrezza (Etna). Rend. Soc. Ital. Mineral. Petrol. 30 (2), 741–770.
Cristofolini, R., Albini, A., Di Girolamo, P., Stanzione, D., 1981. Geochemistry of some volcanic rocks from South-eastern Sicily: rare earth and other trace element distribution. Bull. Volcanol. 44, 95–107.
Cristofolini, R., Ghisetti, F., Scarpa, R., Vezzani, L., 1985. Character of the stress field in the Calabrian arc and southern Apennines (Italy) as deduced by geological, seismological and volcanological information. Tectonophysics 117, 39–58.
De Beni, E., Branca, S., Coltelli, M., Groppelli, G., Wijbrans, J., 2011. $^{39}Ar/^{40}Ar$ isotopic dating of Etna volcanic succession. Ital. J. Geosci. 130, 292–305.
Di Renzo, V., Corsaro, R.A., Miraglia, L., Pompilio, M., Civetta, L., 2019. Long and short-term magma differentiation at Mt. Etna as revealed by Sr-Nd isotopes and geochemical data. Earth Sci. Rev. 190, 112–130.
Di Stefano, A., Branca, S., 2002. Long-term uplift rate of the Etna volcano basement (southern Italy) based on biochronological data from Pleistocene sediments. Terra Nova 14, 61–68.
Dohmen, R., Chakraborty, S., 2007. Fe-Mg diffusion in olivine II: point defect chemistry, change of diffusion mechanisms and a model for calculation of diffusion coefficients in natural olivine. Phys. Chem. Miner. 34, 409–430.
Dohmen, R., Becker, H.W., Chakraborty, S., 2007. Fe-Mg diffusion in olivine I: experimental determination between 700 and 1,200°C as a function of composition, crystal orientation and oxygen fugacity. Phys. Chem. Miner. 34, 389–407.
Ferlito, C., Nicotra, E., 2010. The dyke swarm of Mount Calanna (Etna, Italy): an example of the uppermost portion of a volcanic plumbing system. Bull. Volcanol. 72, 1191–1207.
Franzini, M., Leoni, L., Saitta, M., 1972. A simple method to evaluate the matrix effect in x-ray fluorescence analysis. X-Ray Spectrom. 1, 151–154.
Gennaro, E., Iacono-Marziano, G., Paonita, A., Rotolo, S.G., Martel, C., Rizzo, A.L., Pichavant, M., Liotta, M., 2019. Melt inclusions track melt evolution and degassing of Etnean magmas in the last 15 ka. Lithos 324–325, 716–732.
Ghiorso, M.S., Gualda, G.A.R., 2015. An H_2O-CO_2 mixed fluid saturation model compatible with rhyolite-MELTS. Contrib. Mineral. Petrol. 169, 53.
Ghiorso, M.S., Sack, R.O., 1995. Chemical mass transfer in magmatic processes IV. A revised and internally consistent thermodynamic model for the interpolation and extrapolation of liquid-solid equilibria in magmatic systems at elevated temperatures and pressures. Contrib. Mineral. Petrol. 119, 197–212.
Gillot, P.Y., Kieffer, G., Romano, R., 1994. The evolution of Mount Etna in the light of potassium-argon dating. Acta Vulcanol. 5, 81–87.
Giuffrida, M., Viccaro, M., 2017. Three years (2011−2013) of eruptive activity at Mt. Etna: working modes and timescales of the modern volcano plumbing system from microanalytical studies of crystals. Earth Sci. Rev. 171, 289–322.
Giuffrida, M., Scandura, M., Costa, G., Zuccarello, F., Sciotto, M., Cannata, A., Viccaro, M., 2021. Tracking the summit activity of Mt. Etna volcano between July 2019 and January 2020 by integrating petrological and geophysical data. J. Volcanol. Geotherm. Res. 418, 107350.
Giuffrida, M., Cardone, M., Zuccarello, F., Viccaro, M., 2023. Etna 2011-2022: discoveries from a decade of activity at the volcano. Earth Sci. Rev. 245, 104563.
Gualda, G.A.R., Ghiorso, M.S., Lemons, R.V., Carley, T.L., 2012. Rhyolite-MELTS: a modified calibration of MELTS optimized for silica-rich, fluid-bearing magmatic systems. J. Petrol. 53, 875–890.
Herzberg, C., Asimow, P.D., 2015. PRIMELT3 MEGA.XLSM software for primary magma calculation: peridotite primary magma MgO contents from the liquidus to the solidus. Geochem. Geophys. Geosyst. 16, 563–578.
Hirn, A., Nicolich, R., Gallart, J., Laigle, M., Cernobori, L., ETNASEIS Scientific Group, 1997. Roots of Etna volcano in faults of great earthquakes. Earth Planet. Sci. Lett. 148, 171–191.
Kahl, M., Chakraborty, S., Costa, F., Pompilio, M., Liuzzo, M., Viccaro, M., 2013. Compositionally zoned crystals and real-time degassing data reveal changes in magma transfer dynamics during the 2006 summit eruptive episodes of Mt. Etna. Bull. Volcanol. 75, 692.
Kahl, M., Chakraborty, S., Pompilio, M., Costa, F., 2015. Constraints on the nature and evolution of the magma plumbing system of Mt. Etna volcano (1991-2008) from a combined thermodynamic and kinetic modelling of the compositional record of minerals. J. Petrol. 56, 2025–2068.
Kahl, M., Viccaro, M., Ubide, T., Morgan, D.J., Dingwell, D.B., 2017. A branched magma feeder system during the 1669 eruption of Mt Etna: evidence from a time-integrated study of zoned olivine phenocryst populations. J. Petrol. 58, 443–472.
Kamenetsky, V.S., Clocchiatti, R., 1996. Primitive magmatism of Mt. Etna: insights from mineralogy and melt inclusions. Earth Planet. Sci. Lett. 142, 553–572.
Kamenetsky, V.S., Pompilio, M., Métrich, N., Sobolev, A.V., Kuzmin, D.V., Thomas, R., 2007. Arrival of extremely volatile-rich high-Mg magmas changes explosivity of Mount Etna. Geology 35, 255–258.
Kress, V.C., Carmichael, I.S.E., 1991. The compressibility of silicate liquids containing Fe_2O_3 and the effect of composition, temperature, oxygen fugacity and pressure on their redox states. Contrib. Mineral. Petrol. 108, 82–92.
Le Maitre, R.W., 2002. A Classification of Igneous Rocks and Glossary of Terms. Cambridge University Press, 236 pp.
Métrich, N., Allard, P., Spilliaert, N., Andronico, D., Burton, M., 2004. 2001 flank eruption of the alkali- and volatile-rich primitive basalt responsible for Mount Etna's evolution in the last three decades. Earth Planet. Sci. Lett. 228, 1–17.
Monaco, C., Tapponnier, P., Tortorici, L., Gillot, P.Y., 1997. Late Quaternary slip rates on the Acireale-Piedimonte normal faults and tectonic origin of Mt. Etna (Sicily). Earth Planet. Sci. Lett. 147, 125–139.
Nicotra, E., Viccaro, M., 2012. Unusual magma storage conditions at Mt. Etna (Southern Italy) as evidenced by plagioclase megacryst-bearing lavas: implications for the plumbing system geometry and summit caldera collapse. Bull. Volcanol. 74, 795–815.
Oeser, M., Ruprecht, P., Weyer, S., 2018. Combined Fe-Mg chemical and isotopic zoning in olivine constraining magma mixing-to-eruption timescales for the continental arc volcano Irazú (Costa Rica) and Cr diffusion in olivine. Am. Mineral. 103, 582–599.
Putirka, K., 2016. Rates and styles of planetary cooling on Earth, Moon, Mars, and Vesta, using new models for oxygen fugacity, ferric-ferrous ratios, olivine-liquid Fe-Mg exchange, and mantle potential temperature. Am. Mineral. 101 (4), 819–840.
Rittmann, A., 1973. Structure and evolution of Mount Etna. Philos. Trans. R. Soc. Lond. 274, 5–16.
Shea, T., Lynn, K.J., Garcia, M.O., 2015a. Cracking the olivine zoning code: Distinguishing between crystal growth and diffusion. Geology 43, 935–938.
Shea, T., Costa, F., Krimer, D., Hammer, J.E., 2015b. Accuracy of timescales retrieved from diffusion modeling in olivine: a 3D perspective. Am. Mineral. 100, 2026–2042.
Spilliaert, N., Allard, P., Métrich, N., Sobolev, A.V., 2006. Melt inclusion record of the conditions of ascent, degassing, and extrusion of volatile-rich alkali basalt during the powerful 2002 flank eruption of Mount Etna (Italy). J. Geophys. Res. Solid Earth 111, B04203.
Tanguy, J.C., 1978. Tholeiitic basalt magmatism of Mount Etna and its relations with the alkaline series. Contrib. Mineral. Petrol. 66, 51–67.
Tanguy, J.C., Condomines, M., Kieffer, G., 1997. Evolution of Mount Etna magma: constraints on the present feeding system and eruptive mechanism. J. Volcanol. Geotherm. Res. 75, 221–250.
Viccaro, M., Barca, D., Bohrson, W.A., D'Oriano, C., Giuffrida, M., Nicotra, E., Pitcher, B. W., 2016. Crystal residence times from trace element zoning in plagioclase reveal changes in magma transfer dynamics at Mt. Etna during the last 400 years. Lithos 248-251, 309–323.
Viccaro, M., Giuffrida, M., Zuccarello, F., Scandura, M., Palano, M., Gresta, S., 2019. Violent paroxysmal activity drives self-feeding magma replenishment at Mt. Etna. Sci. Rep. 9, 6717.
Wallace, G.S., Bergantz, G.W., 2003. Constraints on mingling of crystal populations from off-center zoning profiles: a statistical approach. Am. Mineral. 89, 64–73.
Zuccarello, F., Schiavi, F., Viccaro, M., 2021. Magma dehydration controls the energy of recent eruptions at Mt. Etna volcano. Terra Nova 33, 423–429.
Zuccarello, F., Schiavi, F., Viccaro, M., 2022. The eruption run-up at Mt. Etna volcano: constraining magma decompression rates and their relationships with the final eruptive energy. Earth Planet. Sci. Lett. 597, 117821.